WILEY | Hindawi

Research Article

Analysis of the Influence of Fault Fracture Zone on Mining Response Based on FDM-DEM Coupling

Cao Xu [ID], Cao Xiaoshan [ID], Han Tielin [ID], and Ru Yan [ID]

State Key Laboratory Base of Eco-Hydraulic Engineering in Arid Area, Xi'an University of Technology, Xi'an, 710048 Shaanxi, China

Correspondence should be addressed to Han Tielin; s3050210133@163.com

Fault slip will cause a change in mining stress at the longwall face, which will cause adverse effects. In this study, on the basis of Fast Lagrangian Analysis of Continua in 3 Dimensions (FLAC3D) and Particle Flow Code in 3 Dimensions (PFC3D), the sliding of the fault fracture zone and its impact on the longwall working face were analyzed. The rock mass of the fault fracture zone with a certain thickness was constructed using rigid random model particles. The coupling between the wall element of PFC3D and the zone element of the continuous medium in the software was used to realize the transmission of force and displacement, and the interaction between the fault fracture zone and the working face was studied. The influence of the slip of different fault zone positions on the fault and working face was also explored using the method of externally disturbing the fracture zone of the fault. The numerical results showed that as the distance between the fault and the working face continued to decrease, the peak stress concentration in front of the longwall face first increased, then decreased, and gradually shifted to the vicinity of the fault zone. The stress mutation and fault slip occurred within a certain distance of the longwall face from the fault. When fault slip activation begins, the stress near the fault zone showed a sudden change of varying degrees with the advancement of the longwall face. This sudden change was caused by the influence of mining activities from the activation distance of the rock in the fault fracture zone and the rolling extrusion of the rock mass in the fracture zone. When the fault zone closer to the working face was disturbed, the influence on the fault zone and longwall face was greater. When the fault zone near the coal seam was disturbed, the rock mass and working face near the fault zone brought different degrees of dynamic responses, which were mostly instantaneous and had high frequency and amplitude. The results of this research could help in the mining of longwall mining affected by fault zones and have a certain guiding role in coal mining before crossing faults.

1. Introduction

Fault is a type of geological structure often encountered in longwall mining. Underground coal mining will cause redistribution of surrounding in situ stress [1]. Changes in in situ stress may activate nearby faults, resulting in the slip and instability of the faults, and the activity of the faults will affect and bring certain difficulties to the mining of coal [2, 3]. From past experience, the fault slip often leads to coal mine disasters, such as rock bursts [4], water penetration [5], and coal and gas outbursts [6–9]. Therefore, the study of fault slip in coal mining can help in thoroughly under-standing the characteristics of fault slip in underground mines to prevent the risks caused by fault slip.

In previous studies, faults were often treated as plane of weakness [10–12]. The mining subsidence fault layer blocks the stress and energy transfer caused by mining, but in actual geological conditions, faults often appear in the form of fault zones with a certain thickness [13–16]. Wei et al. [17] used the Fast Lagrangian Analysis of Continua in 3 Dimensions (FLAC3D) model to analyze the source mechanism of the fault slip behavior. The postfailure process of the fault slip was studied by constructing a zero-thickness interface element to simulate the fault, and they concluded that

the fault slip shows distinct trends in different positions of the fault. To investigate the sudden failure of faults, Wang et al. [18] performed a physical similarity simulation of a double-fault structure. The simulation results suggested that changes in strain rates from relatively low to abrupt changes may be identified as precursors to fault slip. To study the deformation characteristics of the surrounding rock in the fault zone of a coal mine, Kang et al. [19] established a 3D model of the fault roadway and used special support to treat the roadway and grouting for the fracture, which provided favorable conditions for roadway stability.

Fault planes are often presented in the form of interface element in numerical calculations [20], and fault zones are often replaced with weak interlayer zones; however, most of actual fault zones are discontinuous fragments [21]. Numerical methods are widely used in longwall mining research, and the coupling method of finite difference method (FDM) and discrete element method (DEM) has been well used in geotechnical engineering [22–26]. Li et al. [27] established a 3D coupling model considering both DEM and FDM, simulated ballast particles with DEM considering rolling resistance model, realized the coupling process between DEM and FDM with interface element, and verified the numerical model under impact load through field test. Feng et al. [28] used Particle Flow Code in 3 Dimensions (PFC3D) and FLAC3D to simulate the landslide process. The seismic signal characteristics of the Xiaolin landslide in 2009 were studied and compared with the broadband seismic station data.

The fault slip is caused by the mining activities or a change in tectonic stress. The specific breaking position of the fault is not clear. In this study, the coupling method of FDM and DEM was used to establish a 3D geological fault model. The mining response under the influence of the fault fracture zone was simulated, and the method of external disturbance fault slip was used to deal with the fault fracture zone, to study the response under quasi-static and dynamic conditions, and to provide certain guidance for coal mining under fault conditions.

2. Study Area

Jisan Coal Mine is located in southwest of Jining City, Shandong Province, China. As shown in Figure 1(a), the mine covers an area of $110 \, km^2$. It is estimated that the recoverable coal reserves are 526 million tons. The initial design of the mine type is 5 million tons per year. The output once reached 8 million to 10 million tons per year. The 6303 working face is arranged in the west of the 6300, 6301, and 6302 working faces in the sixth mining area (Figure 1(c)). The designed inclined length is 239.8 m, and the strike length is 2057.8 m. The working face return airway is a gob-side tunnel with a total length of 2114 m and a working face buried depth of 669~711 m. The 6303 return airway is adjacent to the 6302 gob, and the 6302 gob is connected with the 6303 working face return airway. Narrow coal pillars of 2 ~ 3 m are set between them, the average thickness of the coal seam is 4.75 m, and the coal seam is a near-horizontal coal seam. The coal seam column chart is shown in

Figure 1(b). During the advancing process of the working face, rock burst events occurred many times. During the excavation of the return airway along the trough, a total of three faults SF62, SF28, and SF3 were passed, and the fault drops were 1 m, 1.6 m, and 0.5 m, respectively.

3. Establishment and Calculation Scheme of the Numerical Model

3.1. Rock Formation Modeling and Scheme. Using the FED and DEM coupling method for modeling and calculation, Mohr–Coulomb is widely employed in underground engineering analysis [29–31]. The continuum model was selected for the coal pillar and the adjacent complete rock stratum, and the Mohr–Coulomb model was selected for the constitutive relationship of the continuum model. The numerical model was established on the basis of the 6303 working face of the Jisan Coal Mine. The model was a reverse fault, the dip angle of the fault model was 45°, the fault drop was 2 m, and the length $(x) \times$ width $(y) \times$ height (z) of the fault model was $400 \, m \times 10 \, m \times 111 \, m$. The coal seam mining depth was 730 m, the overlying rock could be simplified to a uniform load of 15.7 MPa, and the horizontal stress ratio was 1.5. The model had fixed boundary conditions up, down, front, back, left, and right, and the width of the fault fracture zone was 6 m. If the whole fault zone adopts broken rock, the model cannot be calculated. The fault was replaced with a weakened continuum model below the vertical height of the upper boundary of the model of 16 m. The fracture zone was also replaced with a continuum weakened zone with a vertical height of 14 m above the lower boundary of the model, and the middle part was modeled by broken rock mass. The strata and weakened zone in the model were modeled with finite difference continuous elements. The physical and mechanical parameters of coal and rock were selected with reference to the C8-9 drilling data of the Jisan Coal Mine [32]. The specific parameters are presented in Table 1, and the 3D size of the numerical model is shown in Figure 2.

3.2. Modeling and Parameter Selection for the Fracture Zone. Irregularly shaped gravel was used in the simulation of the fault fracture zone proposed in the numerical model to simulate the discrete properties of the material. In consideration of the force characteristics of the fault zone, the gravel in the crushed zone was assumed to be rigid; that is, it could not be broken again, and a single gravel was regarded as a rigid block that would not fail. PFC3D introduces the method of nonspherical particles. Therefore, the rigid block in the PFC3D software can be used to simulate the fault fracture zone [33]. A single modeling of the fault fracture zone was based on the 3D particle template drawn by CAD, and several random templates were generated using the random film variation coefficient method. The template was imported into the PFC3D software to generate first rigid block particles and then the fault fracture zone. The particle mechanical parameters of the fault fracture zone in the model were selected in accordance with those of gravel in the literature [34]. The computational efficiency for rigid
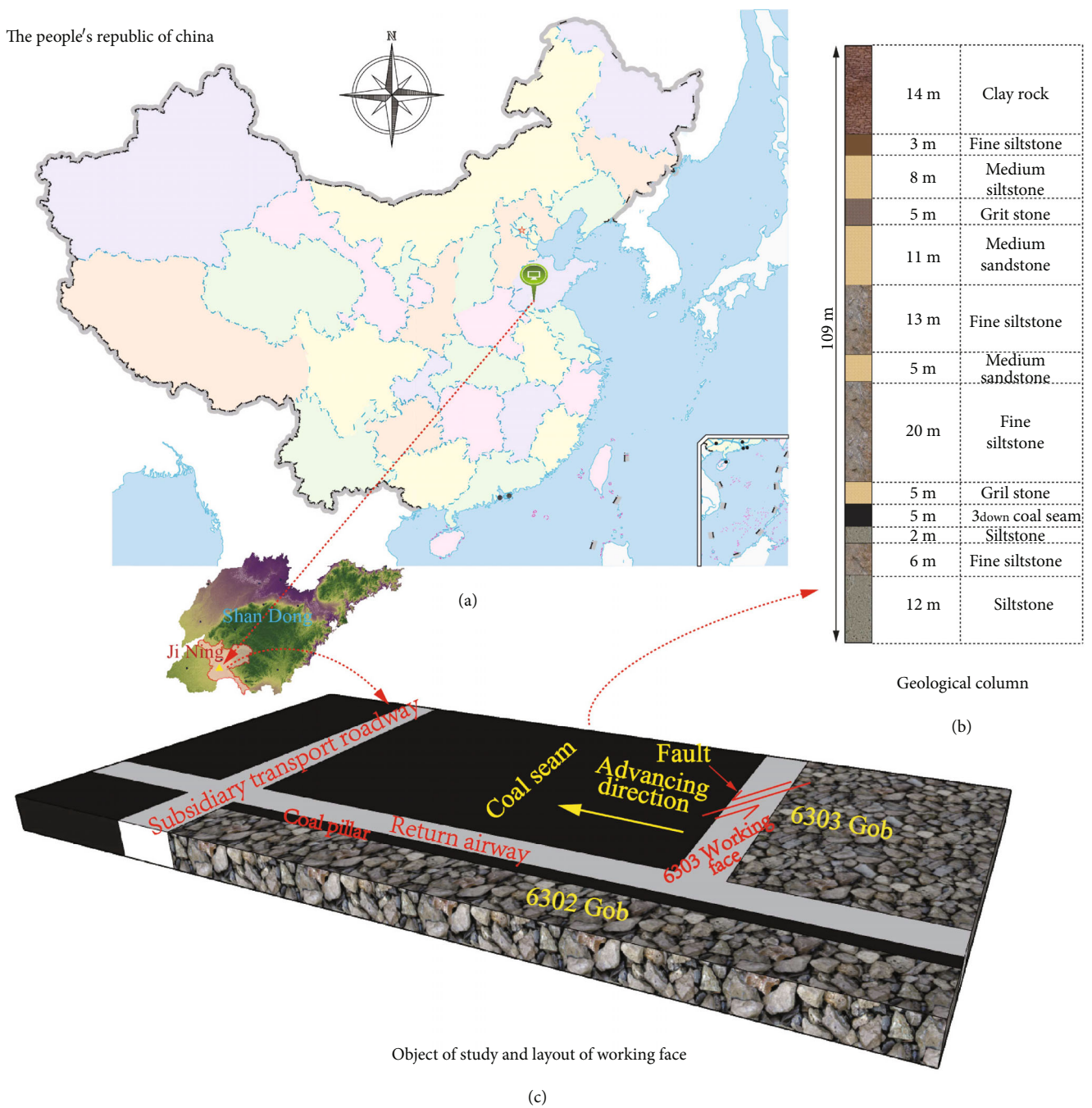
\

(a)

The people's republic of china

Shan Dong

Ji Ning

14 m	Clay rock
3 m	Fine siltstone
8 m	Medium siltstone
5 m	Grit stone
11 m	Medium sandstone
13 m	Fine siltstone
5 m	Medium sandstone
20 m	Fine siltstone
5 m	Gril stone
5 m	3down coal seam
2 m	Siltstone
6 m	Fine siltstone
12 m	Siltstone

109 m

Geological column

(b)

Object of study and layout of working face

(c)

Figure 1: Location of the study area and layout of working face.

blocks was maximized because of the contact detection and resolution of the Gilbert–Johnson–Keerthi algorithm [35], which assumes only one contact between two protruding objects. The simulation of the fault fracture zone is shown in Figure 3. The contact behavior within the fracture zone of the fault was represented using a linear contact bond model that provides a linear spring acting in parallel with two fractured rocks [36], and the specific micromechanical parameters are shown in Table 2. The coupling calculation scheme adopts the wall-element cou-

pling method in FLAC3D [37]. The principle of coupling is to use the contact force and moment of the wall to determine the equivalent force system at the contact point. Force is passed to the grid node along with stiffness, and force and stiffness are logically checked and updated. The updated force and stiffness have changed the geometric parameters and cell stiffness of the solid element to ensure the stability of the calculation process. With reference to the description of the FLAC3D software, in accordance with the parameters of the near elements, the

TABLE 1: Physical and mechanical parameters used in the model.

Name of coal and rock mass	Bulk modulus (GPa)	Shear modulus (GPa)	Density (kg/m³)	Cohesion (MPa)	Internal friction angle (°)
Clay rock	8.2	1.1	2500	1.8	30
Fine siltstone	9.6	3.6	2500	2.5	31
Fine sandstone	23.0	15.2	2700	17.0	38
Coal	1.5	0.8	1420	1.1	25
Grit stone	16.5	7.8	2620	5.0	29
Medium sandstone	19.4	13.2	2700	12.8	40
Siltstone	13.1	4.2	2500	3.0	33
Fault zone	0.5	0.5	2200	0.03	20
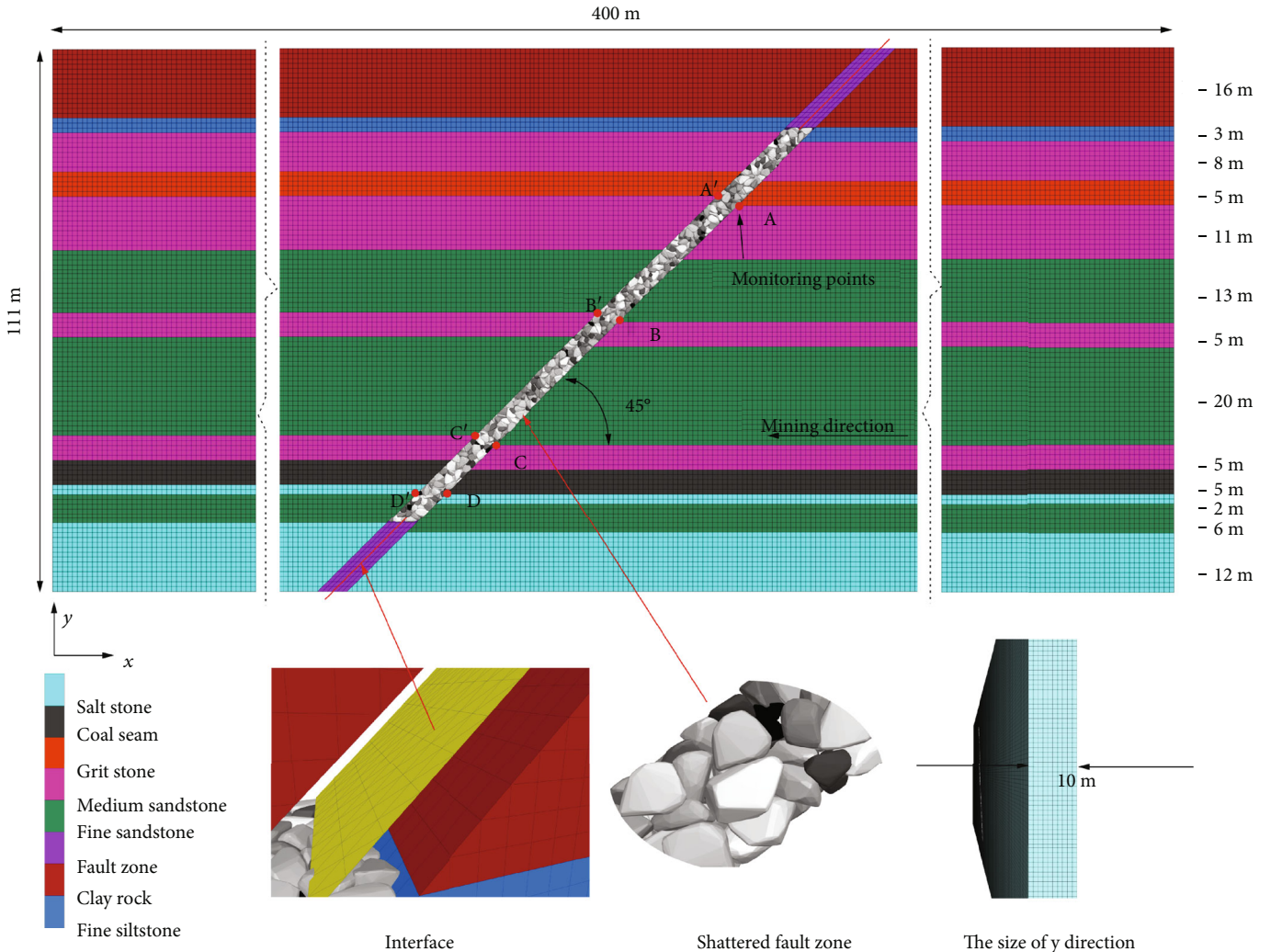
FIGURE 2: 3D dimensions of the numerical model.

parameters of the interface could be based on the equivalent stiffness of the adjacent zone elements, that is,

$$k_{es} = \max \left| \frac{(K + (4/3)G)}{\Delta z_{min}} \right|. \tag{1}$$

The selection was conducted. K is the bulk modulus, G is the shear modulus, and Δz_{min} is the minimum with of adjacent regions in the normal direction. The k_n and k_s of interface parameters is 0.66 MPa, and the value of internal friction angle is 15°.
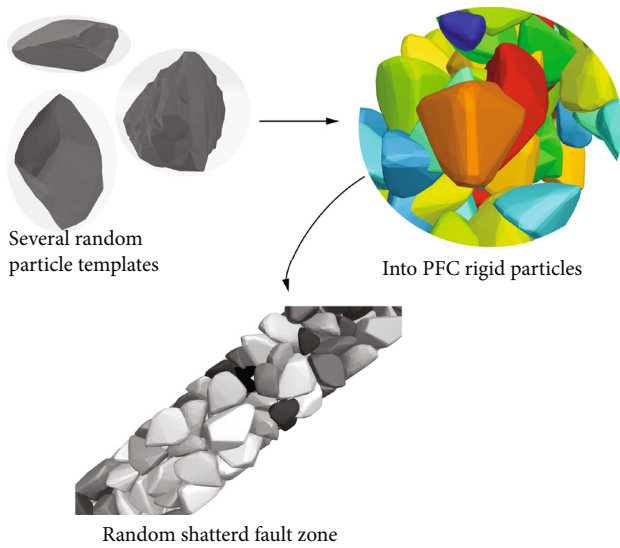
Figure 3: Simulation of the fault fracture zone.

4. Calculation and Mining Influence Analysis under Static Load Conditions

The coal mining method for the working face was the longwall mining method, and the calculation under the static load condition of the model was divided into two parts. First, in situ stress balance of the model was performed. After the in situ stress balance was completed, the overall displacement of the model was initialized to zero. Then, excavation calculation of the coal seam was carried out. The model was excavated from the right boundary, and the farthest distance from the fault plane was 200 m. To observe the stress and fault changes when the working face approaches the fault, the excavation of the model was divided into two stages. In the first stage, the model excavation was 20 m per excavation step within the range of 200–60 m longwall face from the fault. In the second stage, the model excavation was 10 m per excavation step within the range of 60–10 m longwall face from the fault. In the process of coal seam mining, the working face was constantly approaching the fault. The specific excavation design is shown in Figure 4.

4.1. Stress Response Analysis

4.1.1. Coal Seam and Working Face Stress of the Longwall Face. The vertical stress change and nephogram in the coal seam during the mining process in the first stage are shown in Figure 5. During excavation stage 1, due to the distance from the fault zone, the coal seam and working face were less affected by the fault. During the mining process of the longwall face, the vertical stress in the coal seam first increased and then decreased from the longwall face to the fault. The stress peak appeared within a certain distance in front of the longwall face. With the continuous advancement of the longwall face, the stress peak in front of the working face continued to rise. When the coal seam was mined for 20 m, the stress peak of the coal seam was 29.3 MPa at 7 m

in front of the coal wall of the working face. When the coal seam was mined 80 m away from the fault plane, the maximum stress peak at 10 m in front of the working face was 63.4 MPa. As the distance between the working face and the fault decreased gradually, the change trend of stress was small in the range from the working face to the peak stress. In the range from the peak to the fault, the downward trend of stress gradually increased, which was caused by the gradual increase in the stress peak in front of the working face with the continuous advancement of the working face.

The stress change and nephogram in the coal seam during the second stage of coal seam mining are shown in Figure 6, which depicts that the stress change in front of the working face first increased and then decreased, and the stress peak was in front of the working face. However, the peak stress in front of the working face gradually decreased as the distance between the working face and the fault plane decreased. When the longwall face was 60 m away from the fault, the stress peak at 8.5 m in front of the working face was 57.6 MPa; when the working face was 10 m away from the fault, the stress peak at 6.5 m in front of the working face was 21.6 MPa. The stress nephogram illustrates that with the gradual reduction in the distance between the working face and the fault, the stress peak in front of the working face gradually shifted to the vicinity of the fault zone, mainly because the fault zone was a fracture zone. The mining of the working face caused a stress change in the fault fracture zone, slip of the fault zone, and stress release of the fracture zone.

Figure 7 shows the stress peak and the change in its position from the working face during the advancing process of the whole longwall face. When the longwall face was within 200–80 m from the fault, the peak stress gradually increased; when it was within 80–20 m from the fault, the peak stress gradually decreased. As the working face approached the fault, the stress was affected by the fault and tended to rise again. The position of the peak stress in front of the longwall working face gradually increased within 200–100 m, then decreased within 100–30 m, and increased again within 30–10 m of the working face from the fault. That is, when the working face advanced to 60 m or more away from the fault, the stress peak and its position from the working face were affected by the conventional mine pressure. When the working face advanced to 60 m away from the fault and gradually approached the fault, the stress peak of the working face was gradually affected by the fault slip.

4.1.2. Stress Variation along the Fault. The normal stress changes of the eight monitoring points on both sides of the fault zone are shown in Figure 8. From Figure 8(a), the normal stress along monitoring point C below the fault zone (30 m above the coal seam) began to decrease. When the longwall working face advanced from 80 m to 60 m away from the fault, the stress at monitoring point C decreased from 9.96 MPa to 7.72 MPa; when advancing from 60 m to 50 m, the stress decreased from 7.26 MPa to 5.45 MPa. The normal stress of monitoring point C (5 m above the coal seam) under the fault zone began to rise. When the longwall working face was pushed to 80–60 m away from the fault,

TABLE 2: Mechanical parameters in the DEM.

Type	Parameter	Symbol	Value
	Contact Young's modulus	E_c (Pa)	5×10^7
	Normal-to-shear stiffness ratio	k_n/k_s	2.0
Input microparameters	Friction coefficient	μ	0.5
	Gravel size	D (m)	0.25-2 m
	Density	ρ (kg/m^3)	2400
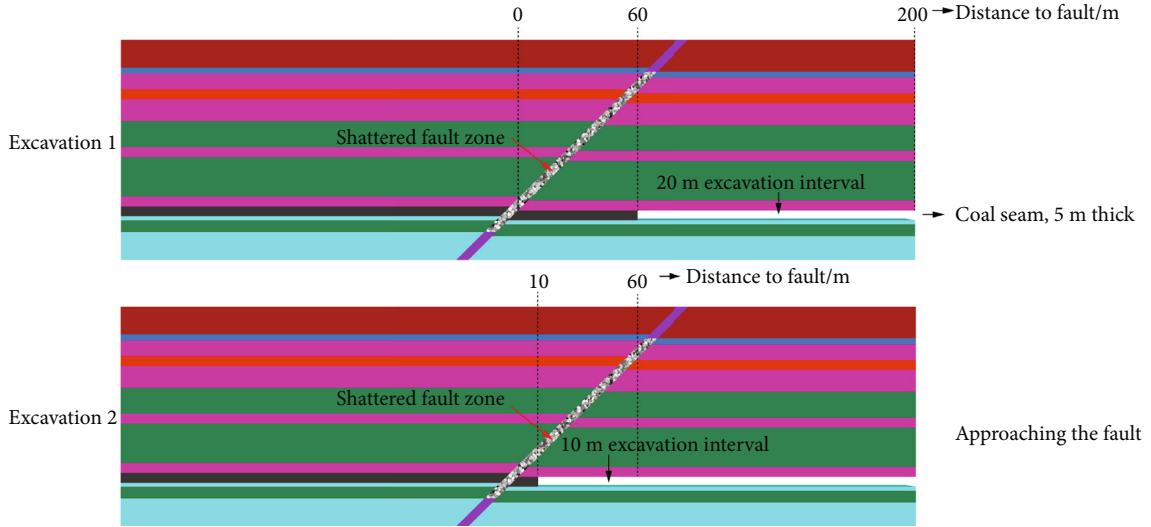
FIGURE 4: Excavation sequence design of the longwall working face.
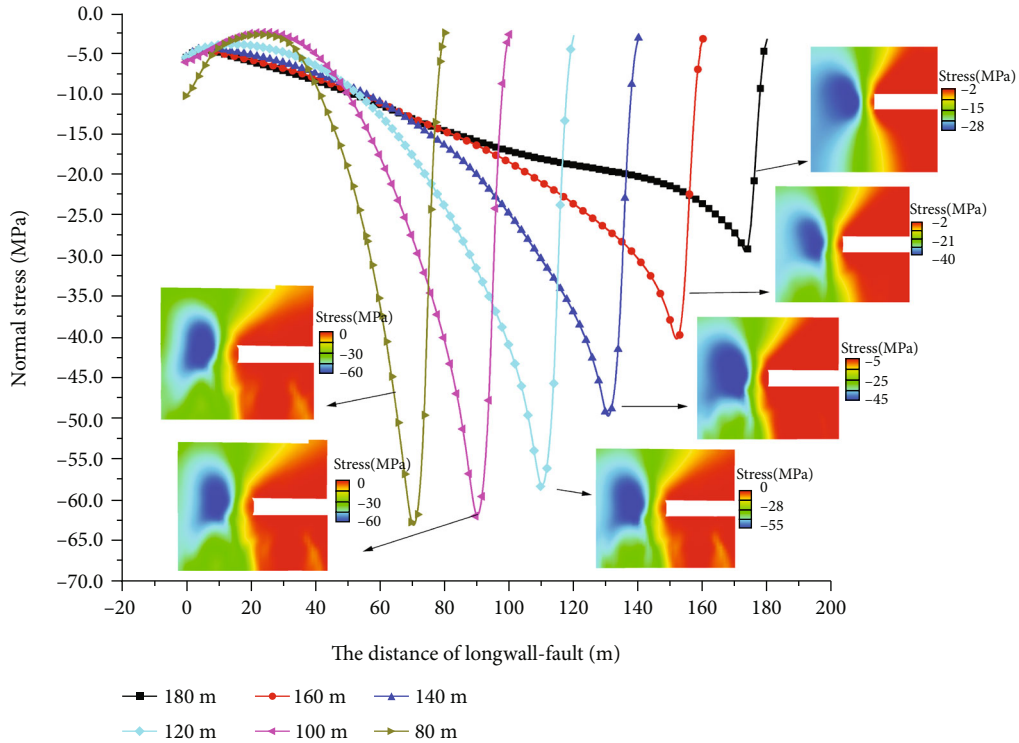
FIGURE 5: Stress and nephogram of the coal seam in excavation stage 1 of the longwall face.
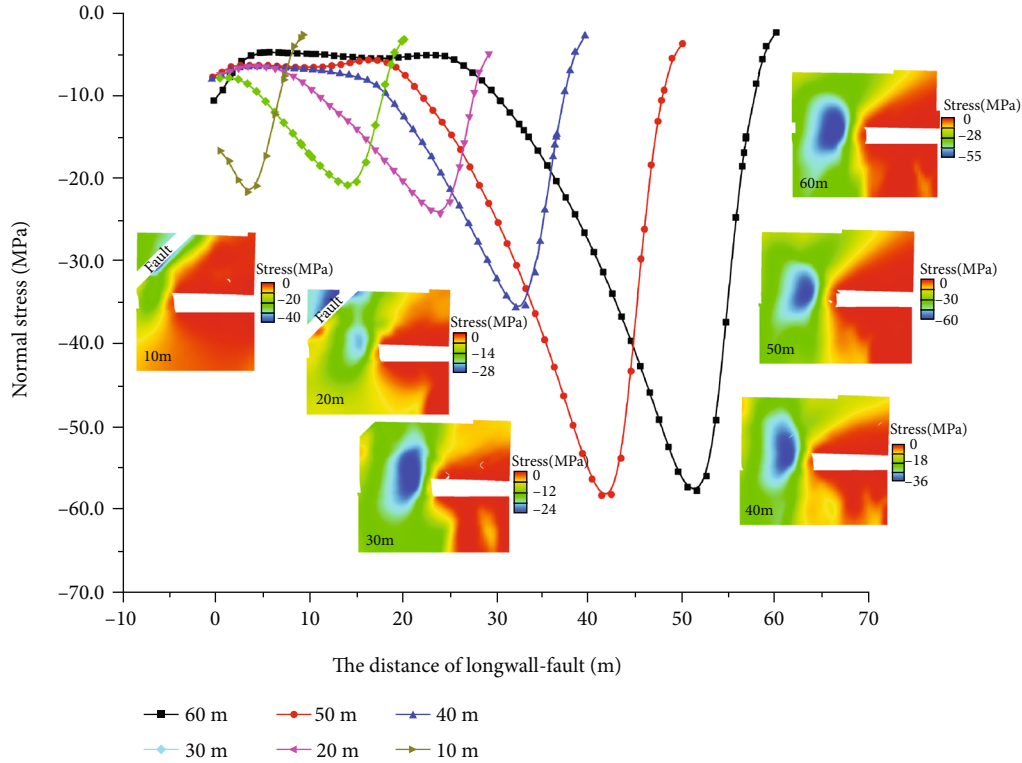
FIGURE 6: Vertical stress and nephogram of the coal seam in excavation stage 2 of the longwall face.
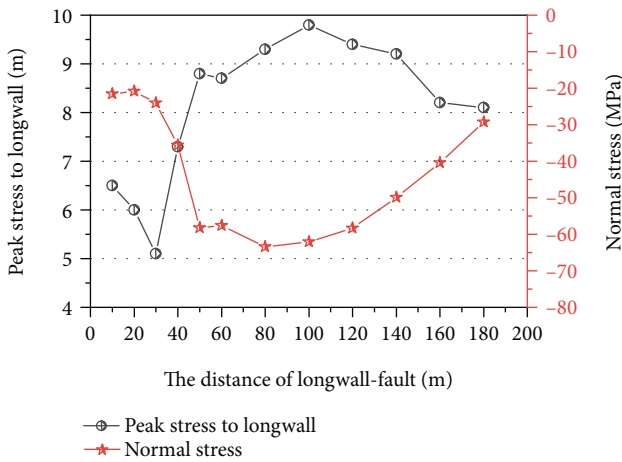

FIGURE 7: Variation in stress peak and position during the advancement of the longwall face.

the stress increased from 5.8 MPa to 8.9 MPa. When the longwall face was pushed to 40 m away from the fault, the stress increased to 16.9 MPa. From the monitoring points below the fault zone, the normal stress remained relatively stable when the longwall face was 80 m or more away from the fault. Affected by the working face mining, the fault slip was caused. The sliding and extrusion of rock mass in the fault fracture zone led to the change in stress on the side of the fault zone. The activation distance of fault slip is when the longwall face is away to 80 m from the fault. When the

working face advanced to the fault range of 40–20 m, the stress of monitoring point B decreased from 16.9 MPa to 6.9 MPa, whereas the stress of monitoring point C increased from 6.48 MPa to 40.8 MPa. Monitoring point D was located on the floor of the coal seam, and the stress changes were not obvious. Figure 8(b) shows the vertical stress of the four monitoring points above the fault zone. When the working face was advanced to 80 m from the fault, the normal stress of the four monitoring points gradually decreased. The change trend of stress at monitoring points A' and C' was the most evident. Specifically, the stress at A' increased from 11 MPa to 22.4 MPa. Meanwhile, the stress at point C' increased from 13.7 MPa to 17.9 MPa when the working face was 80–30 m away from the fault and decreased to 18.5 MPa when advancing to 30–10 m. To sum up, starting from the activation of the fault slip, when the working face advanced to 10 m, the normal stress at monitoring point C, which was 5 m away from the roof, changed the most.

4.2. Displacement Response Analysis. Figure 9 shows the vertical displacement of the eight monitoring points and the displacement difference between adjacent points on both sides of the fadult zone. The fault started from the activation distance, and the displacement of the monitoring points on both sides began to change. Figure 9(a) depicts the vertical displacement of monitoring points A'–A (54 m above the coal seam) and the relative displacement of the two points. The vertical displacement of point A on the right side of the fault fracture zone was more affected by coal seam
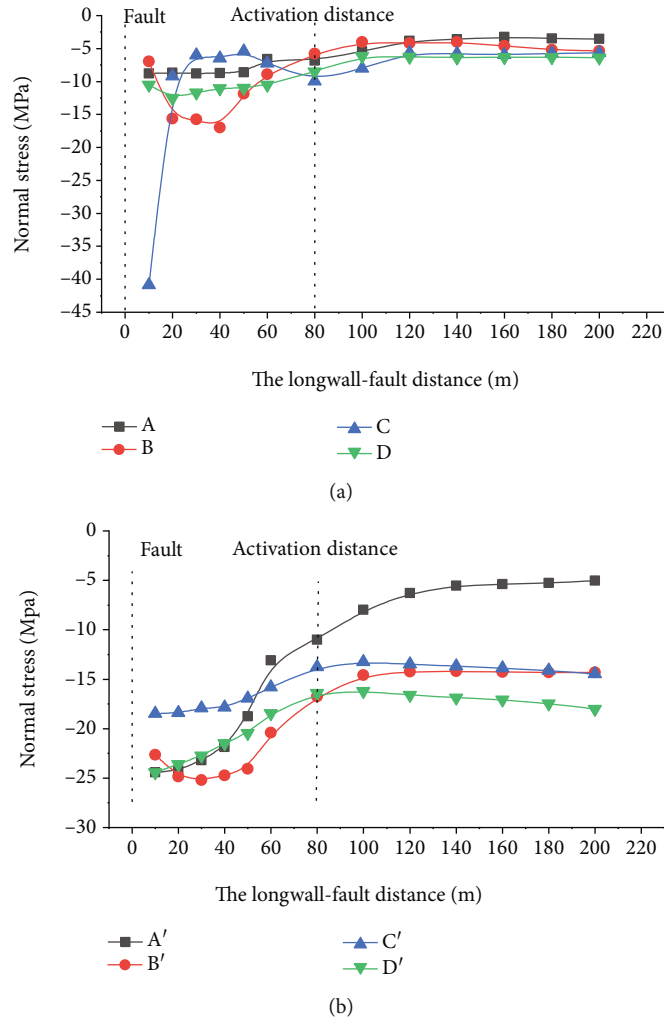
(a)

(b)

FIGURE 8: Normal stress changes at eight monitoring points.

mining than that of point A'. The relative displacement difference between the two points increased continuously from the activation distance of the fault and reached a maximum value of 0.72 m when the longwall face was 10 m away from the fault. The vertical displacement of monitoring points B'–B (30 m above the coal seam) is given in Figure 9(b), and the final displacement difference on both sides of the fault was 0.21 m. The vertical displacement of monitoring points C'–C (5 m above the coal seam) is shown in Figure 9(c). Monitoring point C on the right side of the fault zone started to move upward from the activation distance of the fault when the longwall face was 20 m away from the fault. The overall displacement of point C' was less than that of point C, and the largest displacement slip occurred at the longwall working face 20 m away from the fault, which was 0.21 m. Monitoring points D'–D were located at the bottom of the coal seam. The vertical displacement of the monitoring points on both sides of the fault zone was small. The maximum downward displacement of the left point D' was 0.06 m, and the displacement of the right point D could be ignored, in which the maximum value

was only about 0.003 m. To sum up, for the eight monitoring points of the fault, with shortening vertical distance from the coal seam, the vertical displacement and relative slip on both sides of the fault gradually decreased. The slip of the roof rock stratum was significantly affected by the fault. On the contrary, the floor monitoring points were minimally affected by the fault, and the slip was not obvious.

5. Static Analysis of the External Disturbance Fault Fracture Zone

External disturbance is the main cause of fault slip [34]. Under the condition of fault, underground coal mining may cause fault slip, but the specific slip position of the fault cannot be determined. In previous studies, experiments or numerical simulations were often used to perturb the fault [38, 39]. Observing the slip characteristics of the fault, this study conducted external disturbances in the fault fracture zone. The specific disturbance positions are shown in Figure 10. Disturbances were set at the bottom of the coal seam (disturbance position 1-DP1), the parallel position of
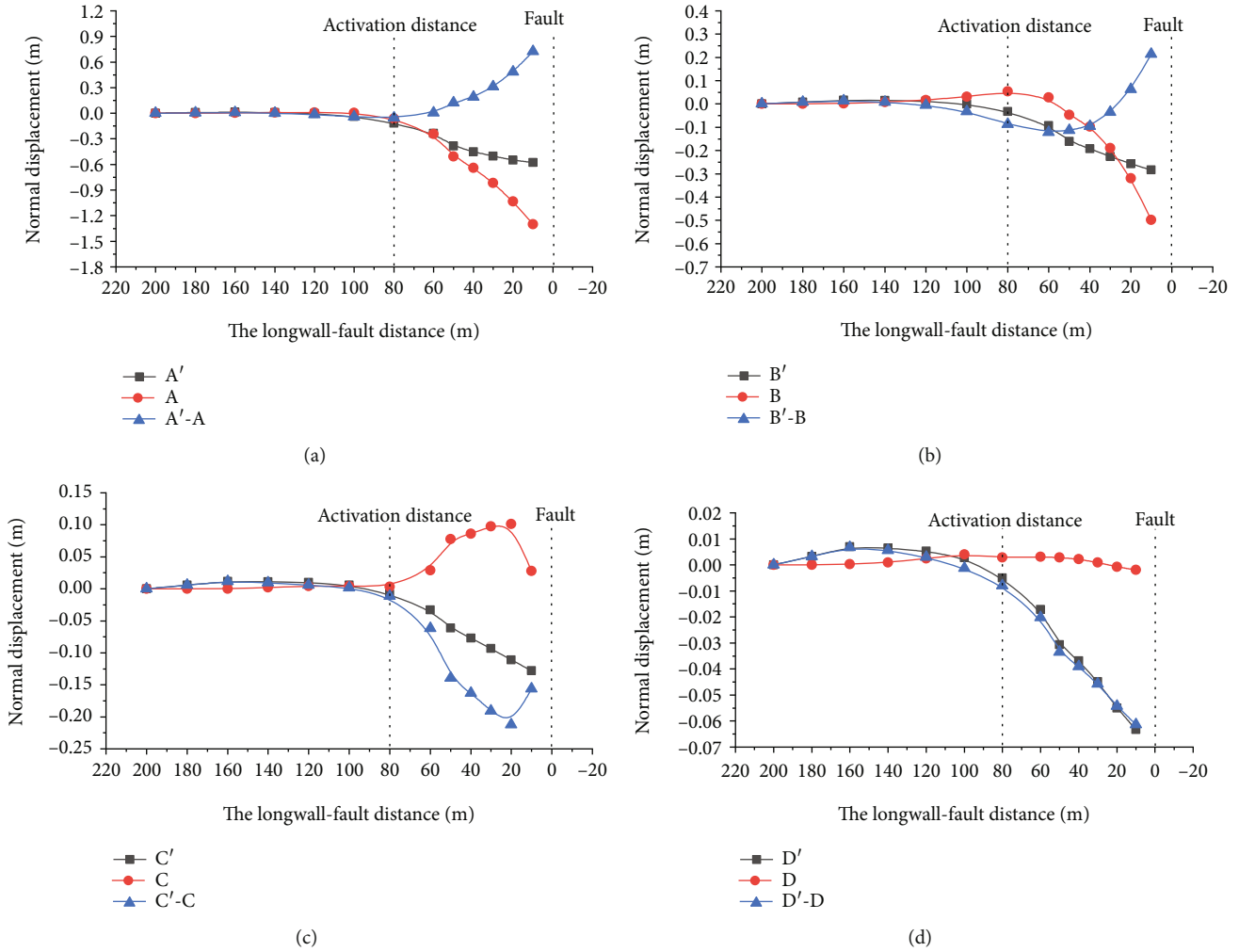
(a)

(b)

(c)

(d)

FIGURE 9: Vertical displacement of eight monitoring points and displacement difference of adjacent points.

the coal seam (disturbance position 2-DP2), the roof of the coal seam (disturbance position 3-DP3), and the roof of the overlying rock layer (disturbance position 4-DP4). Part of the broken rock mass was excavated at the upper and lower positions of the disturbance plane, and the influence of disturbance on coal seam mining and fault slip was observed. The perturbation scheme was to delete the broken rock mass with a diameter of 1.6 m at the upper and lower positions of the perturbation plane, read the undisturbed model data before each perturbation calculation, and observe the influence of different fault sliding positions on the coal seam and the fault.

Figure 11 is the vertical stress variation diagram of four rock stratum monitoring points in the footwall of the fault under external disturbance. Figure 11(a) is the stress variation of point A, which was far away from the coal seam vertically. Owing to the distance from the coal seam and being inconsiderably affected by the mining of the longwall working face, the change in vertical stress under external disturbance was insignificant. Figure 11(b) shows the vertical stress change of monitoring point B of the rock stratum at

a vertical distance of 30 m above the coal seam. This layer of rock was closer to DP4, so DP4 had a more significant influence on the vertical stress of the monitoring point. When the longwall working face was mined to 40 m from the fault, the stress decreased from 16.9 MPa to 14.4 MPa; when the distance was 30 m, the stress decreased from 15.7 MPa to 11.7 MPa. Figure 11(c) illustrates the vertical stress change at monitoring point C (5 m above the coal seam). DP3 had a significant impact on roof rock layer C. When the longwall working face was 60 m away from the fault, the stress during the disturbance dropped by 5 MPa. When the working face was 10 m away from the fault, the stress dropped from 40.3 MPa, which was not disturbed, to 28.2 MPa. The rest of the disturbance points had no significant effect on the vertical stress of the monitoring point. Figure 11(d) shows the change in vertical stress at monitoring point D of the coal seam floor. Except for the farther DP4, which had little influence on the vertical stress of the monitoring point, the three other disturbance points had a certain influence on the vertical stress of this point, especially DP1 and DP2. The maximum stress difference finally
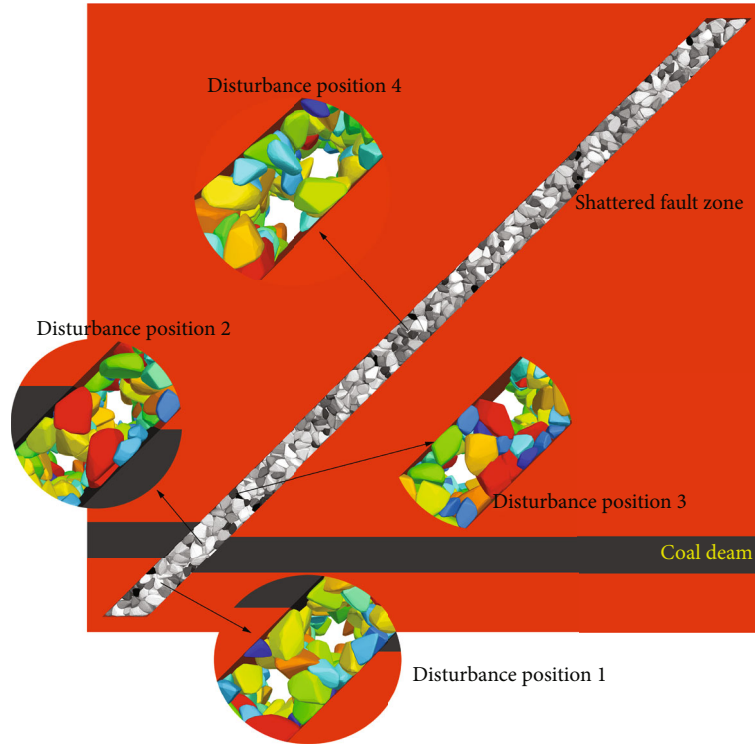
FIGURE 10: Location and scheme of external disturbance points.

generated at DP1 was 8.2 MPa, and the maximum drop of the vertical stress at DP2 was 9.3 MPa compared with the undisturbed one. DP1, DP2, and DP3 exerted a significant impact on the rock formation disturbance near the coal seam. When the slip position of the fault was closer to the coal seam, it might have a greater impact on the stress change near the mining area.

Figure 12 is the vertical stress nephogram of the coal seam and the vicinity of the fault under three external disturbances. The previous calculation indicated that the closer the fault disturbance was to the fault, the more significant the impact would be. DP4, which was far from the vertical height of the coal seam, had little impact on the coal seam, so it had no value. The cloud map was drawn 30 m from the longwall face to 10 m from the fault. Figures 12(a), 12(d), 12(i), and 12(l) are the vertical stress nephograms of the undisturbed and disturbed positions DP1, DP2, and DP3 when the local fault of the longwall working face was 30 m, respectively. Different disturbance points had diverse effects on the stress. In particular, DP1 exerted a minimal effect on the stress concentration in front of the longwall working face, but the overall stress was reduced by 0.2 MPa, which significantly changed the stress under the coal seam near the fault. DP2 slowed down the stress concentration in front of the longwall working face, which increased the stress of the rock mass near the fault with the hanging wall of the fault parallel to the coal seam to a certain extent. DP3 also alleviated the stress concentration in front of the coal wall of the working face, and the position of this stress concentration gradually moved up to the rock

layer of the coal seam roof instead of existing in the coal seam in front. With the continuous advancement of the working face, the distance between the longwall face and the fault was gradually shortened. Under the influence of the fault zone, the stress concentration in front of the coal seam of the working face was reduced, released, and transferred to the fault, and the stress concentration near the fault zone was gradually increased. When the longwall working face was far away from the fault, the stress of the strata in the hanging wall of the fault was higher than that in the footwall. It was also gradually transferred from the hanging wall of the fault to the foot wall of the fault. The reason was that, with the advancement of the longwall face, the size of the complete rock mass between the coal wall and the fault gradually decreased, resulting in a continuous increase in stress and aggravation of stress concentration.

6. Dynamic Response and Seismic Signal Characteristics of Externally Disturbed Fault Zones

The slip of a fault may lead to the occurrence of instantaneous vibrations, such as mine shocks and rock bursts [40, 41]. Dynamic analysis of the model under different disturbance positions was carried out, and the conditions that may cause stress changes were calculated with reference to the above results. The model with a distance of 10 m from the fault on the longwall working face was perturbed, and DP1 and DP2, which were closer to the coal seam, were

(a) Monitoring point A

(b) Monitoring point B

(c) Monitoring point C
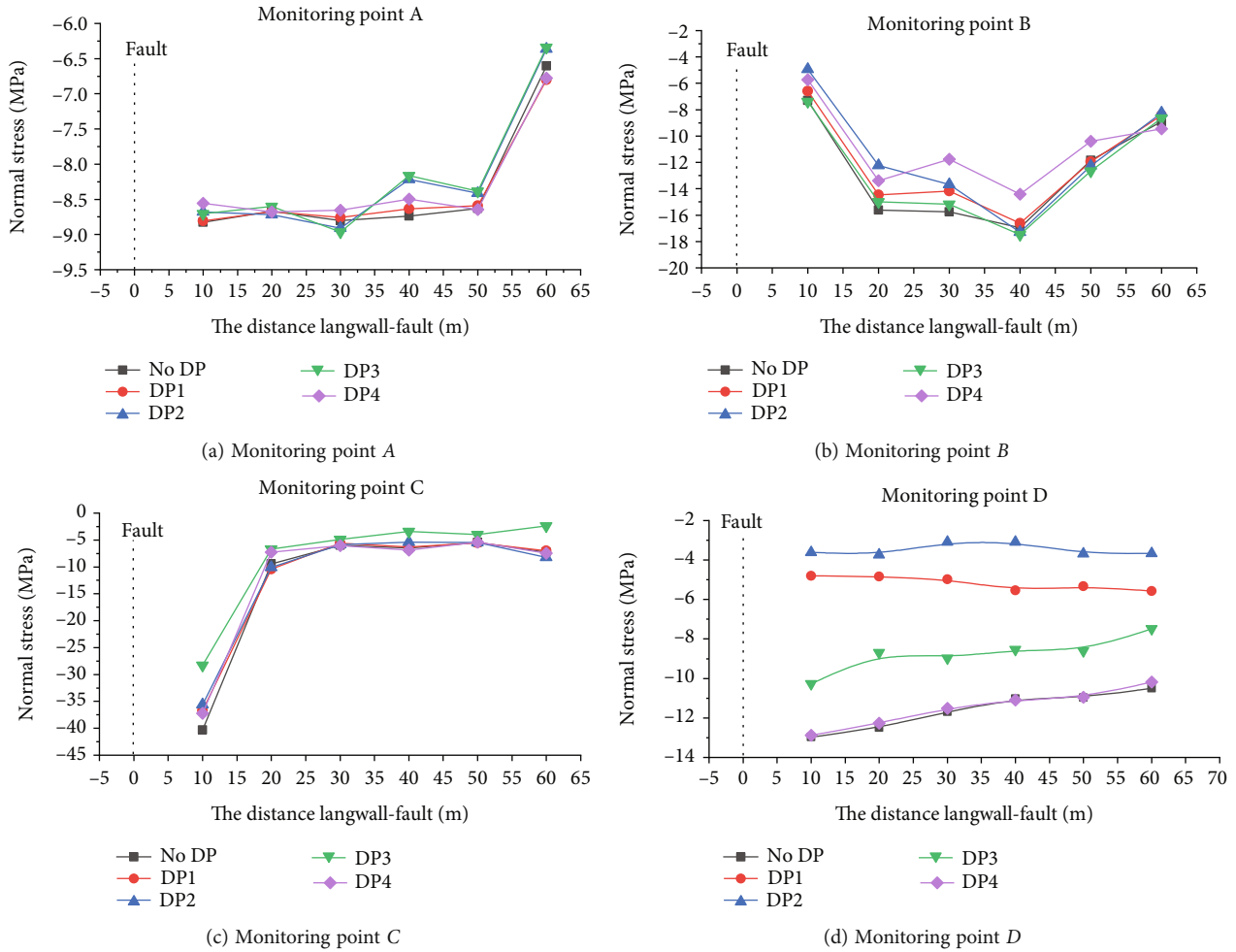
(d) Monitoring point D

FIGURE 11: Vertical stress changes of four monitoring points in the footwall of the fault under external disturbance.

selected for calculation. The influence of the model itself and the factors of the disturbance of the broken zone was disregarded, and dynamic boundary conditions were applied to the model after the broken particles were deleted. No dynamic load was applied to the model, and the acceleration near the fault and the working face was monitored within the dynamic monitoring time of 1 s.

Wavelet transform is the earliest time-frequency signal processing method based on wavelet proposed by Jean Morlet. Wavelet transform can process the signal in time and frequency, accurately grasp the overall characteristics and local details of the signal, and accurately describe the characteristics of nonstationary signals in time-frequency.

Empirical mode decomposition (EMD) is an adaptive time-frequency decomposition method for signal processing proposed by Huang et al. [42], especially for the processing of nonlinear and nonstationary signals. This method processes the signal according to the time characteristics of the signal itself, without setting the odd function in advance. EMD method has been widely used in different engineering fields. The key of EMD is to decompose the complex signal into finite intrinsic mode functions (IMF), and the decom-

posed IMF component is the characteristic signal that characterizes the original signal at different time scales. This method is intuitive, direct, and adaptive.

Figure 13 shows the vertical acceleration, wavelet decomposition time–frequency, and empirical mode decomposition (EMD) maps of the monitoring working face and the vicinity of the fault when the longwall working face was 10 m away from the fault under the disturbance of DP1. Figure 13(a) is the vertical acceleration of the monitoring point near the fault plane. According to the data in the figure, when the fault was disturbed, a large acceleration amplitude occurred within 0.2 s. Therefore, the sliding impact of rock mass in the fault fracture zone had a certain impact on the rock mass, which was instantaneous. In the period after 0.2 s, the acceleration amplitude was small and stable. Figures 13(b) and 13(e) are the time-frequency spectra of the short-time Fourier transform of the acceleration signal. The parts with darker colors were mostly within 0.2 s of the beginning of the calculation, indicating that in this period, the vibration had high amplitude and frequency. Figures 13(c) and 13(f) depict the EMD of the vibration signal. The amplitude of the vibration decreased gradually with
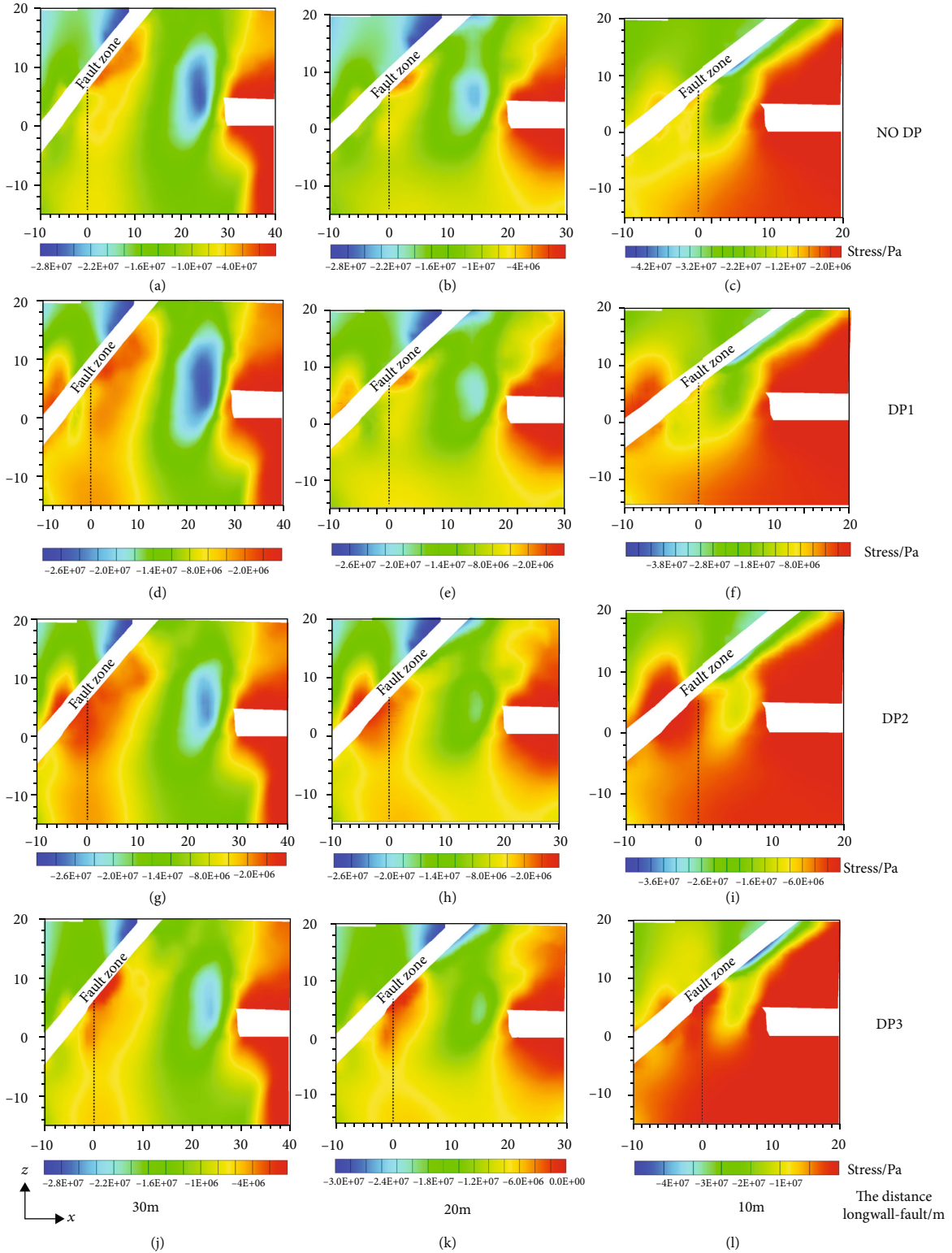
FIGURE 12: Vertical stress nephogram of the coal seam and the vicinity of faults under three external disturbances.

the duration of time, and the high-frequency part of the vibration was mainly concentrated before 0.5 s. The frequency of the vibration also decreased gradually with time. Given that the working face was affected by the overlying rock layer and the fault zone at the same time, the continu-

ous vibration time of the longwall working face was longer than that near the fault zone.

Figure 14 shows the vertical acceleration, wavelet decomposition time–frequency, and EMD maps of the monitored working face and the vicinity of the fault when the
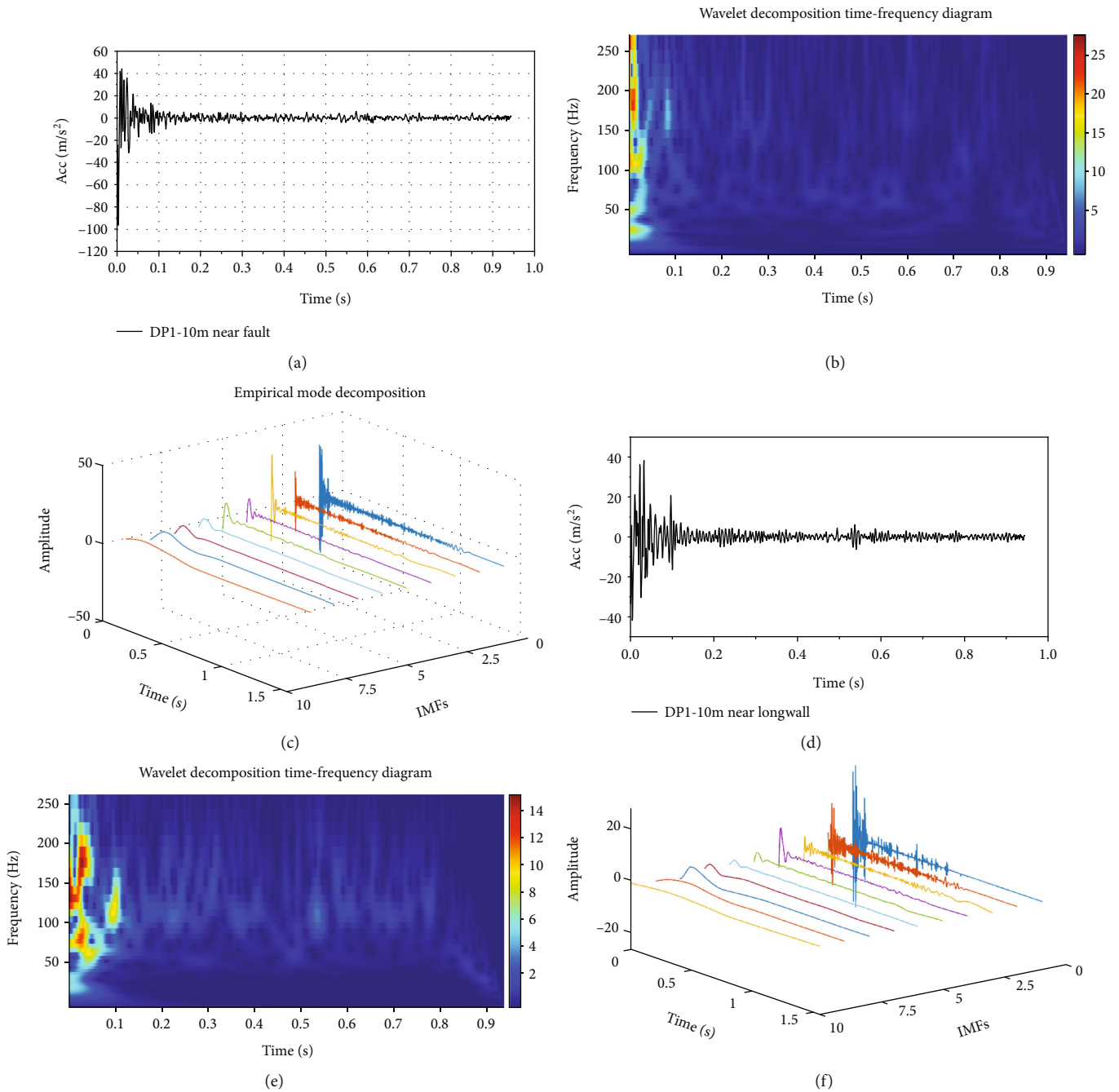
(a)

(b)

(c)

(d)

(e)

(f)

FIGURE 13: Vertical acceleration, wavelet decomposition time–frequency, and EMD maps of the monitored working face and the vicinity of the fault when the longwall working face is 10 m away from the fault under DP1.

longwall working face was 10 m away from the fault under DP2. Figures 14(a) and 14(d) present the vertical acceleration history monitored near the fault zone and near the working face under DP2, respectively. The acceleration amplitude near the fault zone was greater than that near the working face. Given that DP2 was basically parallel to the coal seam, the broken rock mass above the coal seam in the fault zone was disturbed and collapsed, impacting the coal seam near the fault zone and resulting in large vibration near the fault zone. From the time-frequency spectra in Figures 14(b) and 14(e), the high-frequency vibration was also concentrated within 0.2 s of the

onset of the disturbance. As time went on, the vibration frequency decreased. Figures 14(c) and 14(d) show that the vibration amplitude of the model was obvious within 0.5 s at the beginning of the dynamic calculation and continued to weaken with time. DP2 was parallel to the coal seam, resulting in the vibration frequency near the fault zone. Therefore, when the longwall working face was constantly approaching the coal seam, the disturbance effect of the fault zone parallel to the coal seam or the fault zone closer to the coal seam was lower than that of the fault zone on the coal seam floor. The above analysis indicated that the disturbance of the fault zone will produce
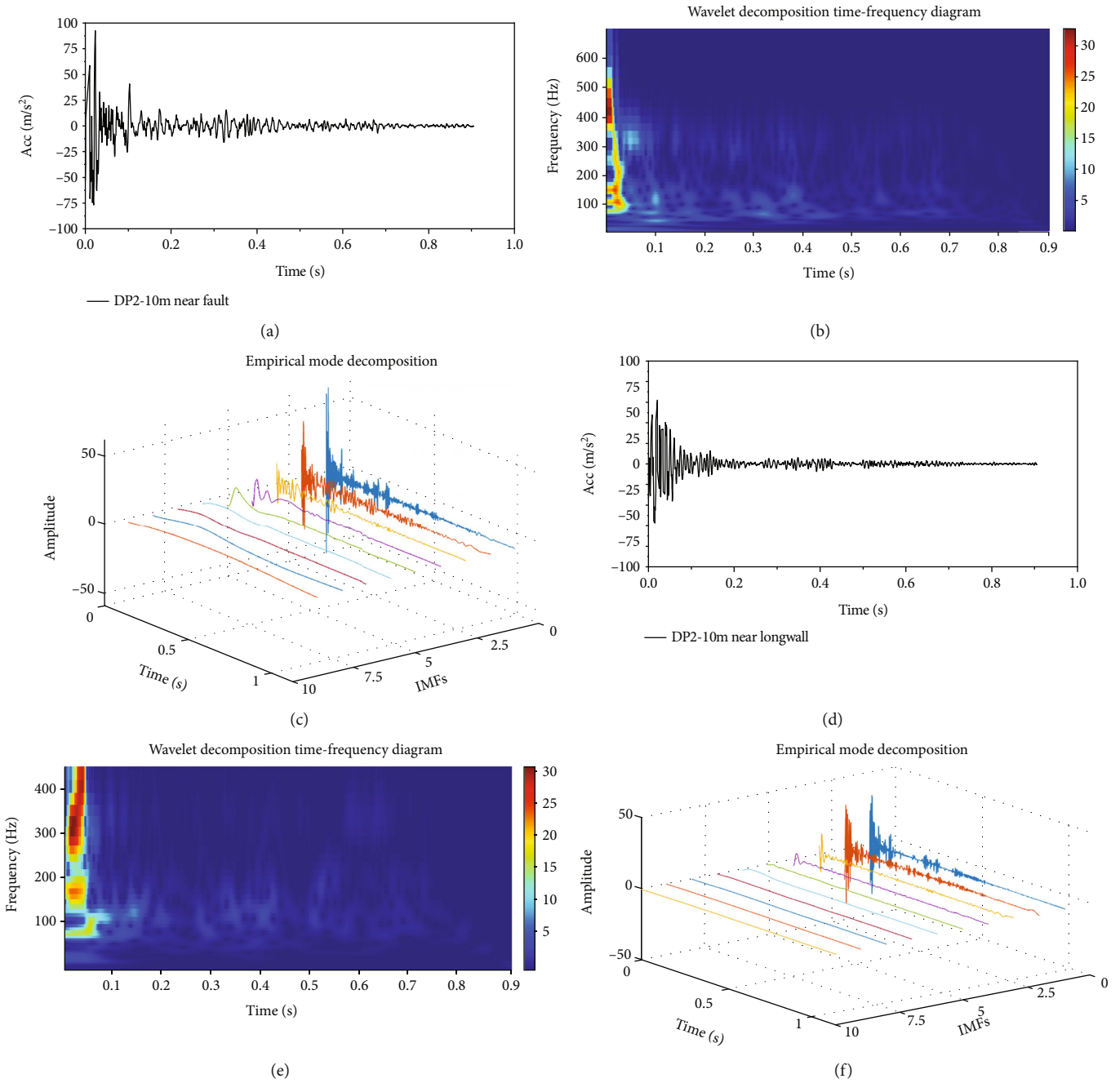
(a)

(b)

(c)

(d)

(e)

(f)

Figure 14: Vertical acceleration, wavelet decomposition time–frequency, and EMD maps of the monitored working face and the vicinity of the fault when the longwall working face is 10 m away from the fault under DP2.

instantaneous vibration when the longwall face approaches the fault, which will affect the mining of coal seams.

7. Conclusions

A FLAC3D–PFC3D-based coupled geological model of continuous discrete media was established, and the fault zone was modeled with discrete media to analyze the influence of the fracture zone of a fault and the sliding mechanism of the fault on longwall mining. The results showed that in the process of the longwall working face approaching the fault zone, the stress peak in front of the longwall face first

increased, then decreased, and finally transferred to the fault fracture zone. Owing to the activation distance of the fault, the monitoring points on both sides of the fault had different degrees of stress mutation. This stress mutation mainly occurred in the rock stratum within 0–30 m of the vertical distance of the coal seam. The rock stratum higher from the vertical distance of the coal seam had greater displacement affected by mining, but no stress mutation occurred. On the contrary, the rock stratum of the coal seam floor was less affected by the fault zone and mining.

Four positions were selected to disturb the fault zone externally to judge the influence of the fault slip at different

positions on the working face and the rock formations near the fault. The numerical results showed that the fault position slip close to the coal seam would have a significant impact on the working face and the fault. This impact was mainly reflected by the sudden drop in stress in the rock stratum near the fault zone, which might cause sudden seismic events. The dynamic response of the disturbance-affected fault zone was monitored. The disturbance-affected faults would produce short-time high-frequency vibrations with large amplitudes.

Data Availability

All data, models, or code generated or used during the study are available from the corresponding author by request (list items).

Conflicts of Interest

The authors declare that they have no conflicts of interest.

Acknowledgments

References

[1] H. Wang, R. Shi, J. Song, Z. Tian, D. Deng, and Y. Jiang, "Mechanical model for the calculation of stress distribution on fault surface during the underground coal seam mining," *International Journal of Rock Mechanics and Mining Sciences*, vol. 144, p. 104765, 2021.

[2] M. R. Islam and R. Shinjo, "Mining-induced fault reactivation associated with the main conveyor belt roadway and safety of the Barapukuria Coal Mine in Bangladesh: constraints from BEM simulations," *International Journal of Coal Geology*, vol. 79, no. 4, pp. 115–130, 2009.

[3] Z. Cao, Q. Gu, Z. Huang, and J. Fu, "Risk assessment of fault water inrush during deep mining," *International Journal of Mining Science and Technology*, vol. 32, no. 2, pp. 423–434, 2022.

[4] H. Xin, Q. Li, L. Liu, Z. Liu, and J. Hou, "Analysis on the influence of fault protection coal pillar size on rockburst," *Geofluids*, vol. 2021, 11 pages, 2021.

[5] J. Shao, F. Zhou, and W. Sun, "Evolution model of seepage characteristics in the process of water inrush in faults," *Geofluids*, vol. 2019, 14 pages, 2019.

[6] W. Li, T. Ren, A. Busch et al., "Architecture, stress state and permeability of a fault zone in Jiulishan coal mine, China: implication for coal and gas outbursts," *International Journal of Coal Geology*, vol. 198, pp. 1–13, 2018.

[7] T. Li, Z. Mu, G. Liu, J. du, and H. Lu, "Stress spatial evolution law and rockburst danger induced by coal mining in fault zone," *International Journal of Mining Science and Technology*, vol. 26, no. 3, pp. 409–415, 2016.

[8] W. Hu, S. Dong, and L. Yan, "Water hazard control technology for safe extractionof coal resources influenced by faulted zone," *Procedia Earth and Planetary Science*, vol. 3, pp. 1–10, 2011.

[9] Q. Wu, M. Wang, and X. Wu, "Investigations of groundwater bursting into coal mine seam floors from fault zones," *International Journal of Rock Mechanics and Mining Sciences*, vol. 41, no. 4, pp. 557–571, 2004.

[10] W. Shiu, Y. Guglielmi, B. Graupner, and J. Rutqvist, "Modelling the water injection induced fault slip and its application to in- situ stress estimation," *International Journal of Rock Mechanics and Mining Sciences*, vol. 137, p. 104537, 2021.

[11] A. Sainoki and H. S. Mitri, "Dynamic behaviour of mining-induced fault slip," *International Journal of Rock Mechanics and Mining Sciences*, vol. 66, pp. 19–29, 2014.

[12] W. Cai, L. Dou, G. Si, and Y. Hu, "Fault-induced coal burst mechanism under mining-induced static and dynamic stresses," *Engineering*, vol. 7, no. 5, pp. 687–700, 2021.

[13] B. Jiang, Y. Zhao, B. Lin, and T. Liu, "Effect of faults on the pore structure of coal and its resultant change on gas emission," *Journal of Petroleum Science and Engineering*, vol. 195, p. 107919, 2020.

[14] L. Lianchong, Y. Tianhong, L. Zhengzhao, Z. Wancheng, and T. Chunan, "Numerical investigation of groundwater outbursts near faults in underground coal mines," *International Journal of Coal Geology*, vol. 85, no. 3-4, pp. 276–288, 2011.

[15] Y. Xue, J. Liu, P. G. Ranjith, Z. Zhang, F. Gao, and S. Wang, "Experimental investigation on the nonlinear characteristics of energy evolution and failure characteristics of coal under different gas pressures," *Bulletin of Engineering Geology and the Environment*, vol. 81, no. 1, pp. 1–26, 2022.

[16] Y. Xue, J. Liu, X. Liang, S. Wang, and Z. Ma, "Ecological risk assessment of soil and water loss by thermal enhanced methane recovery: numerical study using two-phase flow simulation," *Journal of Cleaner Production*, vol. 334, p. 130183, 2022.

[17] C. Wei, C. Zhang, and I. Canbulat, "Numerical analysis of fault-slip behaviour in longwall mining using linear slip weakening law," *Tunnelling and Underground Space Technology*, vol. 104, p. 103541, 2020.

[18] H. Wang, R. Shi, C. Lu, Y. Jiang, D. Deng, and D. Zhang, "Investigation of sudden faults instability induced by coal mining," *Safety Science*, vol. 115, pp. 256–264, 2019.

[19] Y. Kang, C. Hou, J. Liu, Z. Geng, J. Chen, and B. Liu, "Numerical analyses on the stability of a deep coalmine roadway passing through a fault zone: a case study of the Gugui coalfield in China," *Energies*, vol. 14, no. 8, p. 2114, 2021.

[20] C. Wei, C. Zhang, I. Canbulat, and W. Huang, "Numerical investigation into impacts of major fault on coal burst in longwall mining - a case study," *International Journal of Rock Mechanics and Mining Sciences*, vol. 147, p. 104907, 2021.

[21] N. Keulen, R. Heilbronner, H. Stünitz, A. M. Boullier, and H. Ito, "Grain size distributions of fault rocks: a comparison between experimentally and naturally deformed granitoids," *Journal of Structural Geology*, vol. 29, no. 8, pp. 1282–1300, 2007.

[22] Z. Xu, L. Zhang, B. Peng, and S. Zhou, "DEM-FDM numerical investigation on load transfer mechanism of GESC-supported embankment," *Computers and Geotechnics*, vol. 138, p. 104321, 2021.

[23] Z.-Y. Yin, P. Wang, and F. Zhang, "Effect of particle shape on the progressive failure of shield tunnel face in granular soils by

coupled FDM-DEM method," *Tunnelling and Underground Space Technology*, vol. 100, p. 103394, 2020.

[24] C. Shi, C. Zhao, X. Zhang, and Y. Guo, "Coupled discrete-continuum approach for railway ballast track and subgrade macro-meso analysis," *International Journal of Pavement Engineering*, vol. 22, pp. 1–16, 2020.

[25] P. Hou, Y. Xue, F. Gao et al., "Effect of liquid nitrogen cooling on mechanical characteristics and fracture morphology of layer coal under Brazilian splitting test," *International Journal of Rock Mechanics and Mining Sciences*, vol. 151, p. 105026, 2022.

[26] J. Liu, Y. Xue, Q. Zhang, H. Wang, and S. Wang, "Coupled thermo-hydro-mechanical modelling for geothermal doublet system with 3D fractal fracture," *Applied Thermal Engineering*, vol. 200, p. 117716, 2022.

[27] L. Li, W. Liu, M. Ma, G. Jing, and W. Liu, "Research on the dynamic behaviour of the railway ballast assembly subject to the low loading condition based on a tridimensional DEM-FDM coupled approach," *Construction and Building Materials*, vol. 218, pp. 135–149, 2019.

[28] Z. Y. Feng, C. M. Lo, and Q. F. Lin, "The characteristics of the seismic signals induced by landslides using a coupling of discrete element and finite difference methods," *Landslides*, vol. 14, no. 2, pp. 661–674, 2017.

[29] Q. Sun and D. Dias, "Significance of Rayleigh damping in non-linear numerical seismic analysis of tunnels," *Soil Dynamics and Earthquake Engineering*, vol. 115, pp. 489–494, 2018.

[30] J. M. Mayoral and F. A. Flores, "Effects of soil cracking on the seismic response of soil-structure systems," *Soil Dynamics and Earthquake Engineering*, vol. 30, no. 6, pp. 509–523, 2010.

[31] J. M. Mayoral, S. Tepalcapa, A. Roman-de la Sancha, C. S. el Mohtar, and R. Rivas, "Ground subsidence and its implication on building seismic performance," *Soil Dynamics and Earthquake Engineering*, vol. 126, p. 105766, 2019.

[32] Z. H. Li, L. M. Dou, G. X. CHen, H. Jiang, and T. T. Du, "The risk of fault induced rockburst during mining," *Journal of China University of Mining & Technology*, vol. 39, no. 4, pp. 490–495, 2010, 545.

[33] P. A. Cundall, *Itasca Consulting Group Inc, PFC3D version 6.0 users' manual*, 2019.

[34] X. Tan, Z. Hu, C. Chen, and M. Zhao, "3D DEM-FDM coupled analysis of the behavior of an isolated geogrid-encased stone column under axial loading," *Journal of Geotechnical and Geoenvironmental Engineering*, vol. 147, no. 6, p. 04021028, 2021.

[35] E. G. Gilbert, D. W. Johnson, and S. S. Keerthi, "A fast procedure for computing the distance between complex objects in three-dimensional space," *IEEE Journal on Robotics and Automation*, vol. 4, no. 2, pp. 193–203, 1988.

[36] P. A. Cundall and O. D. L. Strack, "A discrete numerical model for granular assemblies," *Géotechnique*, vol. 29, no. 1, pp. 47–65, 1979.

[37] P. A. Cundall, *Itasca Consulting Group Inc, FLAC3D version 6.0 users' manual. PFC plugin*, 2018.

[38] Q. Gan and Q. Lei, "Induced fault reactivation by thermal perturbation in enhanced geothermal systems," *Geothermics*, vol. 86, p. 101814, 2020.

[39] S. Deng, J. Li, H. Jiang, and M. Wang, "Experimental and theoretical study of the fault slip events of rock masses around underground tunnels induced by external disturbances," *Engineering Geology*, vol. 233, pp. 191–199, 2018.

[40] A. Sainoki and H. S. Mitri, "Effect of slip-weakening distance on selected seismic source parameters of mining-induced fault-slip," *International Journal of Rock Mechanics and Mining Sciences*, vol. 73, pp. 115–122, 2015.

[41] A. K. Schwartzkopff, A. Sainoki, and D. Elsworth, "Numerical simulation of mixed aseismic/seismic fault-slip induced by fluid injection using coupled X-FEM analysis," *International Journal of Rock Mechanics and Mining Sciences*, vol. 147, p. 104871, 2021.

[42] N. E. Huang, Z. Shen, S. R. Long et al., "The empirical mode decomposition and the Hilbert spectrum for nonlinear and non-stationary time series analysis," *Proceedings of the Royal Society of London Series A*, vol. 454, no. 1971, pp. 903–995, 1998.